RESEARCH ARTICLE | CHEMISTRY |

Experimental and theoretical evidence for bilayer-by-bilayer surface melting of crystalline ice

M. Alejandra Sánchez, Tanja Kling, Tatsuya Ishiyama, +12 , and Ellen H. G. Backus Authors Info & Affiliations

Edited by Daan Frenkel, University of Cambridge, Cambridge, United Kingdom, and approved November 15, 2016 (received for review August 4, 2016)

December 12, 2016 114 (2) 227-232 https://doi.org/10.1073/pnas.1612893114

VIEW RELATED CONTENT +

PDF

Significance

Over 150 years ago, Faraday discovered the presence of a water layer on ice below the bulk melting temperature. This layer is important for surface chemistry and glacier sliding close to subfreezing conditions. The nature and thickness of this quasi-liquid layer has remained controversial. By combining experimental and simulated surface-specific vibrational spectroscopy, the thickness of this quasi-liquid layer is shown to change in a noncontinuous, stepwise fashion around 257 K. Below this temperature, the first bilayer is already molten; the second bilayer melts at this transition temperature. The blue shift in the vibrational response of the outermost water molecules accompanying the transition reveals a weakening of the hydrogen bond network upon an increase of the water layer thickness.

Abstract

On the surface of water ice, a quasi-liquid layer (QLL) has been extensively reported at temperatures below its bulk melting point at 273 K. Approaching the bulk melting temperature from below, the thickness of the QLL is known to increase. To elucidate the precise temperature variation of the QLL, and its nature, we investigate the surface melting of hexagonal ice by combining noncontact, surface-specific vibrational sum frequency generation (SFG) spectroscopy and spectra calculated from molecular dynamics simulations. Using SFG, we probe the outermost water layers of distinct single crystalline ice faces at different temperatures. For the basal face, a stepwise, sudden weakening of the hydrogen-bonded structure of the outermost water layers occurs at 257 K. The spectral calculations from the molecular dynamics simulations reproduce the experimental findings; this allows us to interpret our experimental findings in terms of a stepwise change from one to two molten bilayers at the transition temperature.

As early as 1859, Faraday proposed the existence of a liquid-like layer at ice surfaces (1, 2). This surface-induced ice melting represents one of the most prominent examples of an interface-induced premelting phase transition (3, 4). During the last decades, the so-called quasi-liquid layer (QLL) at the ice−air interface, wetting the crystalline bulk phase, has been studied by theory (5), computer simulations (6–8) and various experimental techniques (9–17). Despite the general agreement on the presence of a QLL below the bulk freezing point, the temperature-dependent thickness of the QLL has remained controversial. The experimentally reported onset temperature for QLL formation varies between 200 K and 271 K. Moreover, most experimental work shows that, with increasing temperature, the QLL thickness gradually and continuously increases from the onset temperature up to the bulk melting point, with reported thicknesses varying from 2 nm to over 45 nm at 271 K (3, 11–13, 15, 16, 18). In contrast, early simulations showed that the QLL is formed in a more quantized, bilayer-by-bilayer manner (8).

We provide evidence of layer-by-layer growth of the QLL at the ice−air interface by combining experiments with simulations. We use surface-specific vibrational sum-frequency generation (SFG) spectroscopy. Our experimental data are corroborated by spectral calculations based on molecular dynamics (MD) simulations. SFG spectra provide unique information on the vibrational response of the outermost molecules of a centrosymmetric solid, such as the proton-disordered ice studied here. At the interface, the symmetry is broken, thus allowing us to specifically probe the vibrational response of the interfacial region. The signal is strongly enhanced when the infrared laser pulse is resonant with a molecular vibration (19). The amplitude of the signal depends on the number of vibrational chromophores and its transition dipole moment, the amount of order present at the interface, and intramolecular/intermolecular coupling effects.

Therefore, SFG spectroscopy has been used for unveiling the molecular conformation of the ice−air interface. Shen and coworkers (20, 21) focused on the frequency region of the nonhydrogen-bonded OH stretch mode (3,600 cm^{-1} to 3,800 cm^{-1}) in the temperature range from 173 K to 271 K. By probing these OH groups, which stick into the air, they concluded that surface disordering appears at temperatures as low as 200 K. The Shultz group (22–25) studied the hydrogen-bonded OH stretch frequency region (3,200 cm^{-1} to 3,600 cm^{-1}) of various basal and prism faces of the ice−air interface at temperatures around 100 K.

To study surface melting, we focus here on the hydrogen-bonded part of the spectrum between 235 K and 273 K where, according to most reports (18), surface melting takes place. As the frequency of the OH stretch vibration depends on the hydrogen bond strength with neighboring molecules (26, 27), the SFG spectrum contains information on the intermolecular interactions between water molecules at the surface; this allows us to determine the hydrogen bond strength at the interface and to obtain information about the QLL.

In this study, we explore mainly the surface melting of the basal plane of hexagonal ice (ice Ih), which is the most common ice phase. In ice Ih, the oxygen atoms are located in the wurtzite structure. The hydrogen atoms are arranged according to the Bernal−Fowler ice rules (28). Depending on the orientation of the ice crystal, different crystallographic planes are exposed to air. Top and side views of the basal plane (0001), a primary prism plane $(10\bar{1}0)$, and a secondary prism plane $(\bar{1}2\bar{1}0)$ are schematically shown in Fig. 1 and Table S1. In the direction perpendicular to the basal and primary prism planes, the oxygen atoms form a bilayer structure. In contrast, in the direction perpendicular to the secondary prism plane, oxygen layers are equidistant.

Fig. 1.

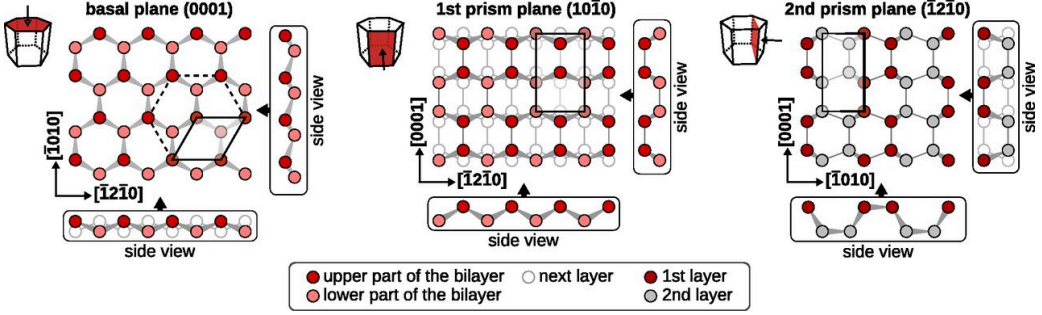

High symmetry faces of ice Ih. Top view of the basal (Left), primary prism (Center), and secondary prism (Right) face of ice Ih. Circles represent oxygen atoms. The crystallographic unit cell is highlighted by solid black lines. Dashed lines and Insets indicate the hexagonal symmetry. For the basal and primary prism plane, dark and light red circles represent oxygen atoms in the upper and lower part, respectively, of the bilayer. For the secondary prism plane, the first (dark red) and second (gray) layers are shown. Shaded circles indicate the positions of oxygen atoms in underlying layers. At the surface, each "upper molecule" (either upper part of the bilayer or of the first layer) contributes exactly one dangling OH bond.

Table S1.

Selection of accessible Bragg reflections for different surface orientations of ice Ih

Reflection	2θ	q, Å^{-1}	$q_{\parallel}$ Å^{-1}	$q_{\perp}$, Å^{-1}	δ	ω	χ	φ
Basal								
(00.2)	24.29°	1.716	0	1.716	12.15°	12.15°	0°	—
(10.5)	68.38°	4.584	1.613	4.290	54.80°	13.58°	0°	0°
(10.5)	68.38°	4.584	1.613	4.290	54.80°	13.58°	0°	60°
Primary prism								
(10.0)	22.81°	1.613	0	1.613	11.41°	11.41°	0°	—
(20.0)	46.60°	3.226	0	3.226	23.30°	23.30°	0°	—
(30.0)	72.78°	4.840	0	4.840	36.39°	36.39°	0°	—
(40.0)	104.57°	6.453	0	6.453	52.29°	52.29°	0°	—
(20.1)	48.32°	3.338	0.858	3.226	39.05°	9.27°	0°	0°
(20.$\bar{1}$)	48.32°	3.338	−0.858	3.226	39.05°	9.27°	0°	180°
Secondary prism								
(11.0)	40.06°	2.794	0	2.794	20.03°	20.03°	0°	0°
(22.0)	86.49°	5.588	0	5.588	43.24°	43.24°	0°	0°
(22.2)	91.56°	5.846	1.716	5.588	62.85°	28.71°	0°	0°
(22.$\bar{2}$)	91.56°	5.846	−1.716	5.588	62.85°	28.71°	0°	180°

Wavelength 1.541 Å, angular sector 0° < δ + ω < 125°, γ = 0, α = 0, −10° < ω < 55°, −15° < χ -90° < 15°, 0° < φ < 360°. Lattice parameters a = 4.498 and c = 7.322 were taken from Fortes et al. (64).

To obtain well-defined ice samples, single crystals were grown from a melt using the seed extraction method (29, 30) based on the Czochralski process (31) (Fig. S1). Cylindrical ice single crystals (60 mm diameter, 30 mm length) were obtained by slowly withdrawing the seed from the melt. Single crystallinity was checked using crossed polarizers in a Rigsby stage (32). Samples with different surface orientation

were characterized by Formvar etching (Fig. S2) and X-ray diffraction (Fig. S3 and Table S2). Details on ice growth and characterization can be found in *Materials and Methods* and *Supporting Information*.

Fig. S1.

Single crystalline ice. (A) Picture of the experimental ice-growing machine showing the seed and supercooled melt. (B) Ice between two crossed polarizers; only one big domain is observed in the single crystalline sample. (C) Cross-section of the SFG measuring cell.

Fig. S2.

Images of the basal, primary prism, and secondary prism plane after Formvar etching. The red bar represents 50 μm.

Fig. S3.

Rocking curve of the (30.0) reflection measured at the primary prism surface (symbols). The red curve represents a fit of a pseudo Voigt function to the experimental data.

Table S2.

Orientation of selected ice samples (different from the ones used for the SFG experiments) oriented by Formvar etching as shown in Fig. S2

Sample	$\Delta\omega$	$\Delta\chi$	$\Delta\varphi$
Basal	1.0°	0.9°	5.0°
Primary prism	3.9°	2.9°	4.6°
Secondary prism	5.6°	0.2°	0.4°

Results and Discussion

Fig. 2 displays the SFG spectra under *ssp* polarization (*s*, SFG; *s*, visible; *p*, IR) of the basal ice face at different temperatures. See *Materials and Methods* and Fig. S4 for details of the SFG experiments. An intense peak slightly below 3,200 cm^{-1} is observed, which agrees with the previous SFG measurements (21). As the temperature increases from 235 K to 264 K, the intensity decreases by a factor of 5. Similar trends are observed for the secondary prism face of ice (Fig. S5). Wei et al. (21) reported a similar, albeit much weaker, intensity decrease by a factor of 3 with increasing temperature from 173 K to 272 K. In contrast, a strong temperature dependence has been reported by the Shultz group. They observed an intensity decrease by approximately a factor of 6 in the temperature range from 113 K to 178 K (24). The decrease in the ice SFG intensity with increasing temperature has previously been interpreted as a decrease in the (bulk-allowed) quadrupole contribution (22, 33) and a loss in the tetrahedral hydrogen bond structure leading to a decrease in the intermolecular coupling (34, 35).

Fig. 2.

Ice–quasi-liquid–air interface studied with SFG. (A) SFG spectra under ssp polarization between 235 K and 273 K for the basal face of ice Ih. The black lines are the experimental results; the red lines are results of the two component fit (see Results and Discussion). The data are offset for clarity. (B) First moment of the spectral intensities shown at different temperatures for the basal and secondary prism face averaged over up to four different experiments. The lines are sigmoidal fits through the data points. (C) Contribution of the 235 K and 269 K spectra to the SFG spectra at intermediate temperatures, for the basal face. Typical error bars based on reproducibility from experiment to experiment are given in the graph.

Fig. S4.

Laser influence on ice sample. Shown are SFG spectra in the hydrogen-bonded OH stretch region of the basal face at 235 K at different irradiation conditions. The SFG signal is stable in time and has similar intensity and spectral shape at 250 and 164 Hz.

Fig. S5.

Ice–quasi-liquid–air interface study with SFG. (A) SFG spectra between 235 K and 273 K for the secondary prism plane. The black lines are the experimental result; the red lines are the results of the fit. (B) Contribution of the 235 K and 269 K spectra to the SFG spectra at intermediate temperatures.

Besides the intensity variation [$I(\omega)$], Fig. 2*A* also shows an apparent shift of the hydrogen-bonded OH stretch band to higher-frequency (ω) with increasing temperature. To quantify the frequency shift as a function of temperature, the numerically determined first moment of the spectral distribution, $\int \omega I(\omega) d\omega / \int I(\omega) d\omega$, of the hydrogen-bonded OH peak has been plotted in Fig. 2*B*. Surprisingly, the first moment of the spectral distribution exhibits not a gradual shift with increasing temperature but rather a steep increase from ~3,185 cm^{-1} to ~3,210 cm^{-1} around 257 K. A sigmoidal fit gives the transition temperature at 256.9 ± 0.3 K (i.e., −16 °C). For the secondary prism face (*c* axis oriented perpendicular to plane of incidence), we also observe a decrease in intensity and a shift to higher frequency with increasing temperature (Fig. 2*B*), whereas the observed shift is smaller than that for the basal face. A sigmoidal fit results in a transition temperature at 258.6 ± 0.1 K (i.e., −14 °C). As a higher frequency of the OH stretch mode of water indicates a weakening of the hydrogen bonds' strengths (26, 27), the sigmoidal shape may be interpreted as an abrupt weakening of the hydrogen bonds in the top layers of the ice sample for both the basal and, although smaller, the secondary prism face.

Interestingly, the spectra between 235 K and 269 K can be very well described by a linear combination of the spectra at 235 and 269 K, where the higher temperature spectrum is blue shifted. The relative

fits (red curves in Fig. 2*A*) are plotted in Fig. 2*C*. Only the amplitude of the 235 and 269 K spectral contribution are free parameters. The contribution of the 235 K spectrum decreases linearly with increasing temperature, whereas the contribution of the 269 K spectrum has a stepwise increase from zero to a finite value around 254 K.

Besides the hydrogen-bonded OH stretch region, the vibrational response of OH bonds sticking out of the surface, i.e., dangling OHs, also contains potentially important information about the nature of the surface. The vibrational frequency of this mode is rather high, around 3,700 cm^{-1}, as the OH group does not form a hydrogen bond. Fig. 3*A* shows the SFG spectra in the frequency range from 3,630 cm^{-1} to 3,760 cm^{-1} for various temperatures that reveal a moderate, continuous reduction of the free OH intensity with increasing temperature. The peak amplitude can be obtained by calculating the peak area between 3,630 cm^{-1} and 3,760 cm^{-1}. As apparent from the data in Fig. 3*B*, the amplitude of the 3,700 cm^{-1} mode shows only a weak, continuous temperature dependence, indicating that the outermost surface structure does not change dramatically, in agreement with previous results by Shen and coworkers (20). The secondary prism face shows the same trend.

Fig. 3.

SFG spectra of the basal face in the free OH region. (A) SFG spectra from 3,630 cm^{-1} to 3,760 cm^{-1} at different temperatures. Data are offset for clarity; the solid lines are to guide the eyes. Note that, due to different acquisition time and laser power, the intensity cannot be compared with the intensity in Fig. 2A. (B) Spectra area of the free OH vibration vs. temperature.

To connect the experimental results to a molecular-level picture, MD simulations were performed using the TIP4P/Ice model, showing the melting point at 272.2 K (36). The details of the simulation are given in *Materials and Methods* and *Supporting Information*. Fig. 4 and Fig. S6 show the density profiles for different temperatures for the basal and secondary prism faces. The double peaks for basal face and a single peak for prism face manifest the bilayer structure for the basal face and the single-layer structure for the secondary prism face, respectively. The observed density profiles resemble those reported in previous works (7, 8). At 230 K, the density profile for the slab cleaved along the basal plane displays a double peak structure for all bilayers, except the outermost bilayer, indicating that the outermost layer is already disordered at this temperature. This trend is also supported by the radial distribution function (RDF), which, for the outer layer, is similar to the water reference, whereas it retains the structure of ice from the second layer inward (Fig. S7). The double peak fine structure in the second layer suddenly disappears between 260 K and 270 K. At the same temperature, the RDF for the second layer loses crystalline features and turns liquid-like. Moreover, the exchange of water molecules between the layers increases around this temperature. The orange lines in Fig. 4 and Fig. S7 mark the molten layers based on the absence of the double peak structure in the density profile and the liquid features of the RDF. These

findings of Kroes (8). The density profiles of the slab exposing the secondary prism face show that melting occurs gradually, as the difference between density peaks and valleys in the surface layers decreases progressively.

Fig. 4.

Density profiles. Density profiles obtained with the TIP4P/Ice model for (A) the basal and (B) the secondary prism plane of ice Ih, illustrating the bilayer and monolayer structure, respectively. For the basal plane at 250 K, only the outer bilayer has lost its characteristic density profile, whereas, at 270 K, the outer two bilayers are molten, as indicated by the orange color. The density profile for the secondary prism face, with equal distance between the layers, changes gradually, as indicated by a gradual transition of the envelope from a rectangular to an elliptical shape. Additional temperatures are depicted in Fig. S6. Molten (orange) vs. crystalline (black) layers are identified by (bi)layer by (bi)layer RDFs (Fig. S7).

Fig. S6.

Density profiles. Density profiles for the (A) basal and (B) secondary prism planes at temperatures between 230 K and 272 K.

Fig. S7.

RDFs. (A) Temperature-dependent RDFs of reference ice Ih systems and liquid water. The reference samples for ice Ih contain 1,536 water molecules. The reference systems for the liquid system contain 480 water molecules. (B and C) Temperature-dependent RDFs for the (B) first and (C) second bilayer of the basal plane of ice Ih.

Subsequently, SFG spectra are calculated to connect the molecular-level changes to the spectrum. The modeling details can be found in *Materials and Methods* and in *Supporting Information*. Fig. 5*A* shows the calculated *ssp* polarized SFG intensity spectra of the basal face of ice as a function of temperature in the hydrogen-bonded and the dangling OH regions of the spectrum. In the simulations, only the first two outer bilayers were taken into account. The inner bilayers were assumed not to contribute to the SFG signal, because they have inversion symmetry, which can be seen from the orientation of the O−H group plotted in Fig. 6. At low temperature (Fig. 6*A*), the distribution is symmetric ("up" and "down") for the third

bonding stretching band has a relatively intense peak in the SFG spectrum near 3,200 cm^{-1}. Similar to the experiments, with increasing temperature, the peak intensity decreases and the peak maximum appears to shift toward higher frequencies. As evident from Fig. 5*B*, a sigmoidal fit through the peak maximum of hydrogen-bonded OH stretch mode as a function of temperature results in an inflection point at 252 ± 1 K (i.e., −21 °C). This temperature is slightly lower than the temperature observed in the density profiles reported in Fig. 4. However, these simulations were performed using a different force field (see *Supporting Information* for details). Also in agreement with the experiments, the dangling OH band at about 3,700 cm^{-1} shows a moderate reduction with increasing temperature (Fig. 5*C*).

Fig. 5.

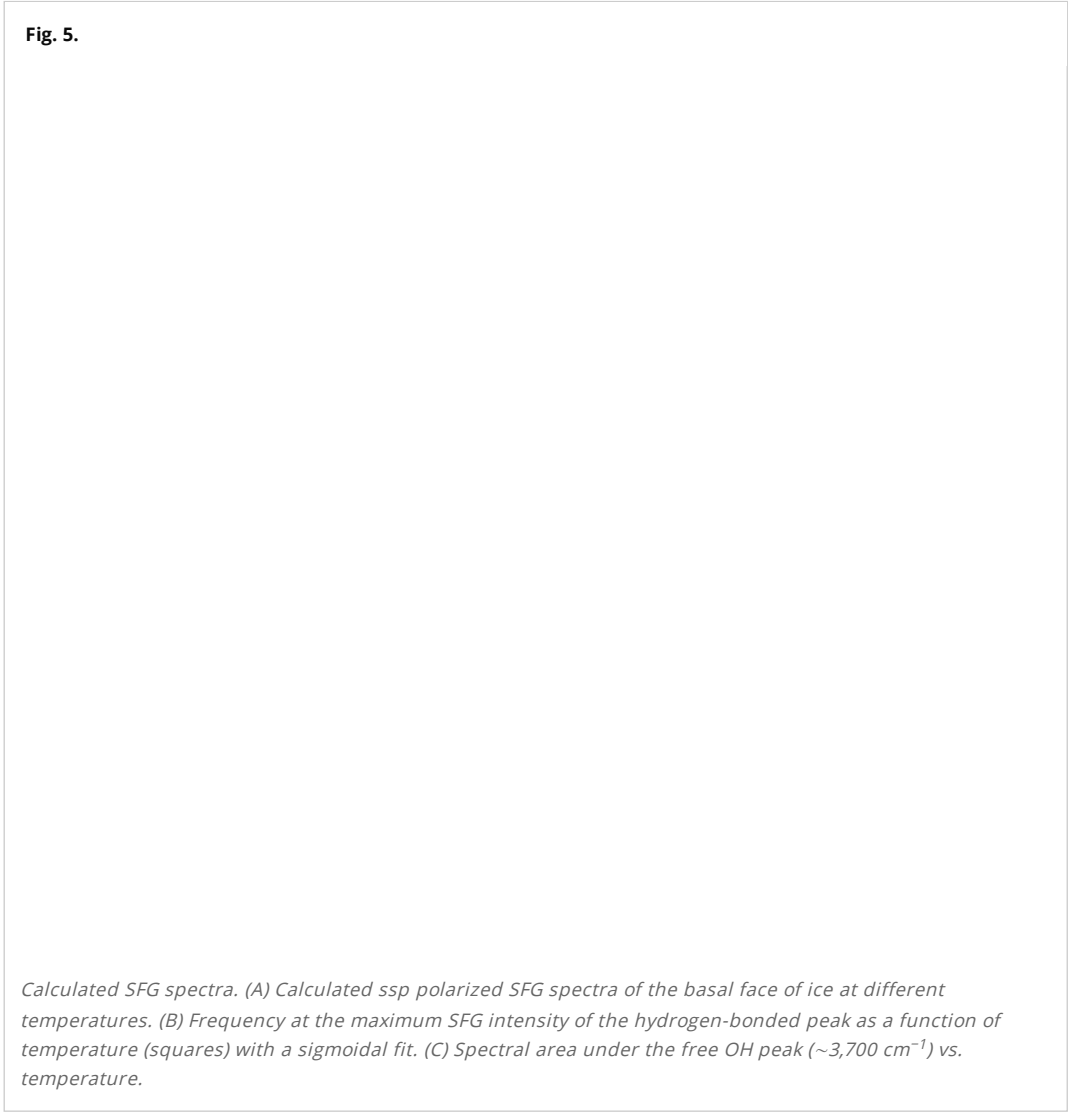

Calculated SFG spectra. (A) Calculated ssp polarized SFG spectra of the basal face of ice at different temperatures. (B) Frequency at the maximum SFG intensity of the hydrogen-bonded peak as a function of temperature (squares) with a sigmoidal fit. (C) Spectral area under the free OH peak (~3,700 cm^{-1}) vs. temperature.

Fig. 6.

O−H groups orientation. (A and B) Orientation distribution of the water OH groups for the first three bilayers at (A) 230 K and (B) 270 K. (C) Maxima of the orientation distribution of up- and down-pointing OH groups in the second bilayer around cos θ = 0.3 (red) and −0.3 (blue) as a function of temperature. (D) Definition of angle θ, so that OH groups are pointing up and down, for, respectively, positive and negative cos θ.

A more detailed look into the orientation of the water molecules provides more details on the molecular origin of the temperature-dependent change in the calculated SFG signal. Fig. 6*C* shows the two maxima for the probability distributions of up- and down-oriented O−H groups of the water molecules of the second bilayer. Clearly, the probability maximum decreases with increasing temperature as the water becomes more disordered, making the distribution wider and the maximum consequently lower. However, this change is not continuous: between 250 K and 260 K, the slope of the curves in Fig. 6*C* alters, reflecting a larger change of the disorder of the orientation of the water molecules for a given temperature step, apparently caused by melting of the second bilayer.

Both experimentally measured and calculated spectra show an abrupt blue shift of the spectral response, indicating a weaker hydrogen bond environment, consistent with a transition to a state with more liquid-like character. These theoretical results explain the experimentally observed sudden change in the SFG spectra, and thus the interfacial water organization, around 257 K in terms of a transition from one to two molten bilayers. Because of the discreteness of the ice lattice, it is reasonable that the variation of the QLL with increasing temperature occurs in a discrete manner, i.e., in a bilayer-by-bilayer fashion. “Patches” of molten bilayers in large crystalline samples would be thermodynamically unfavorable, as there would be a penalty from the liquid−solid interface. Hence, we attribute the observed change to the transition of the QLL thickness from one to two bilayers. Interestingly, such a transition seems to have been observed as well by photoelectron spectroscopy experiments; the inferred thickness seems to suddenly change between 248 K and 258 K but was not investigated in more detail (10). Layer by layer melting has been found for other systems (37, 38). In particular, for crystals with directional bonds, tendencies for layering are pronounced (39). However, for most of these systems, blocked surface melting, i.e., a finite thickness of the QLL up to the bulk melting point, has been observed (37). In contrast, for ice with its tetrahedral H-bonded structure, at low temperature, we observe a sharp transition from one to two layers, i.e., an

the layer thickness has been reported (10, 12–14, 16). Therefore, water seems to be one of the few cases showing stepwise melting at low temperature and diverging melting at higher temperature.

From our experimental SFG data alone, we cannot strictly exclude that the observed transition represents the onset of surface melting, i.e., solid ice below 257 K and a QLL layer with constant or increasing thickness above 257 K, instead of the formation of one QLL layer to two QLL layers. Indeed, using gracing incidence X-ray diffraction, Dosch and coworkers (13, 16) found onset temperatures of 259.5 K (−13.5 °C) for the basal and 260.5 K (−12.5 °C) for nonbasal surfaces. Although the transition temperatures are slightly lower in our experiments, we find the same trend, i.e., a lower transition temperature for the basal compared with the prism face. However, this alternative interpretation is not only at odds with the simulations presented above, it is also in seeming contradiction of the experimental observation that the response from the dangling OH groups varies modestly and continuously over our temperature window. It is unlikely that the dangling OH groups of solid ice and those of water in the QLL have the same exact vibrational frequency. Moreover, one would expect not only a frequency shift but also an intensity change, as the fast reorientational motion that is possible for the free dangling OH groups (40) in the QLL is expected to significantly affect the vibrational response. Indeed, previous SFG results have witnessed a change in the order parameter of the dangling OH at 200 K, which is a measure of the disorder of the surface. Below 200 K, the order parameter is constant, whereas, above 200 K, the order parameter decreases with increasing temperature (20). The picture that thus emerges is that the first bilayer melts at temperatures as low as 200 K, and that surface melting proceeds from 257 K onward. Although our results indicate that a single additional bilayer melts at this temperature, we cannot exclude a continuously increasing thickness of the QLL above this temperature.

The spectral changes associated with the transition provide information about the change in the local environment of the water molecules. Comparing the spectral response at 235 K and that at 269 K, the former has a strong contribution from ice and likely a (small) contribution from the very thin QLL present already at 235 K. The high temperature spectrum has a larger contribution of the QLL, as this spectrum originates from a state with at least two molten bilayers, and contains a smaller contribution from the ice, as the ice signal decreases in amplitude with increasing temperature. The analysis of the temperature-dependent spectra reveals that the contribution of the 235 K spectrum goes down with increasing temperature as the tetrahedral hydrogen bond structure in ice gets more disordered with increasing temperature. As the number of water layers abruptly increases at 257 K, so does the central frequency of the spectral response (Figs. 2*B* and 5*B*). The shift to higher frequency of the 269 K spectrum compared with the 235 K spectrum indicates a weakening of the hydrogen bonds for the QLL layer compared with ice. For the free OH groups, the small gradual decrease observed in both the experimental and the calculated SFG spectra could indicate a small decrease in ordered free OH groups with increasing temperature and/or an increased rotational mobility of these groups.

The stepwise change in the SFG spectrum observed for the basal face is also observed for the secondary prism face, albeit with a smaller, less pronounced frequency change in the experimental spectra (Fig. 2*B*). Also, the transition in the contribution of the 269 K spectrum after fitting the data with a linear combination of the spectra at low and high temperatures is less pronounced (Fig. S5). A possible explanation for the smaller step may be that, for the secondary prism face, single layers of ice melt, as the layer−layer interaction does not give rise to bilayer behavior for this crystal cut.

Although it is clear that as the temperature increases the SFG response shifts to higher frequency, a key question is about the nature of the QLL: Is it spectroscopically discernible from liquid water? To answer this question, we compare, in Fig. 7, the normalized SFG spectra from supercooled water and ice, both recorded at 269 K. The supercooled water spectrum looks similar to water spectra above zero degrees, indicating little difference between the surfaces of supercooled water and water at ambient

Fig. 7.

SFG spectra of ice and supercooled water. Normalized SFG spectra of supercooled liquid water (green/blue) and ice, both at 269 K (orange/red), and ice at 243 K (gray/black). The lines are to guide the eye.

For the ice surface at 269 K, we expect to probe both the ice−QLL and QLL−water interfaces. The response differs substantially from that of the supercooled water−air interface. The two spectra look very similar around 3,200 cm^{-1} (the small difference at low frequency can at least in part be attributed to a higher relative contribution of NR signal at 269 K than at 243 K), but, between 3,300 cm^{-1} and 3,500 cm^{-1}, the relative intensity in the ice spectrum is much lower than that of the supercooled water. The ice spectrum at 269 K resembles more the ice spectrum at 243 K than the supercooled water spectrum. This comparison could suggest that, at 269 K, the ice−QLL interface still significantly contributes to the observed SFG spectrum and/or that the QLL has a different nature than supercooled water in the sense that it has stronger hydrogen bonds, possibly due to templating from the underlying crystalline ice order. However, Fig. S8 shows only a slight increased ordering, i.e., tetrahedrality, for the outmost layer of ice compared with liquid water (280 K in Fig. S8) in the MD simulations.

Fig. S8.

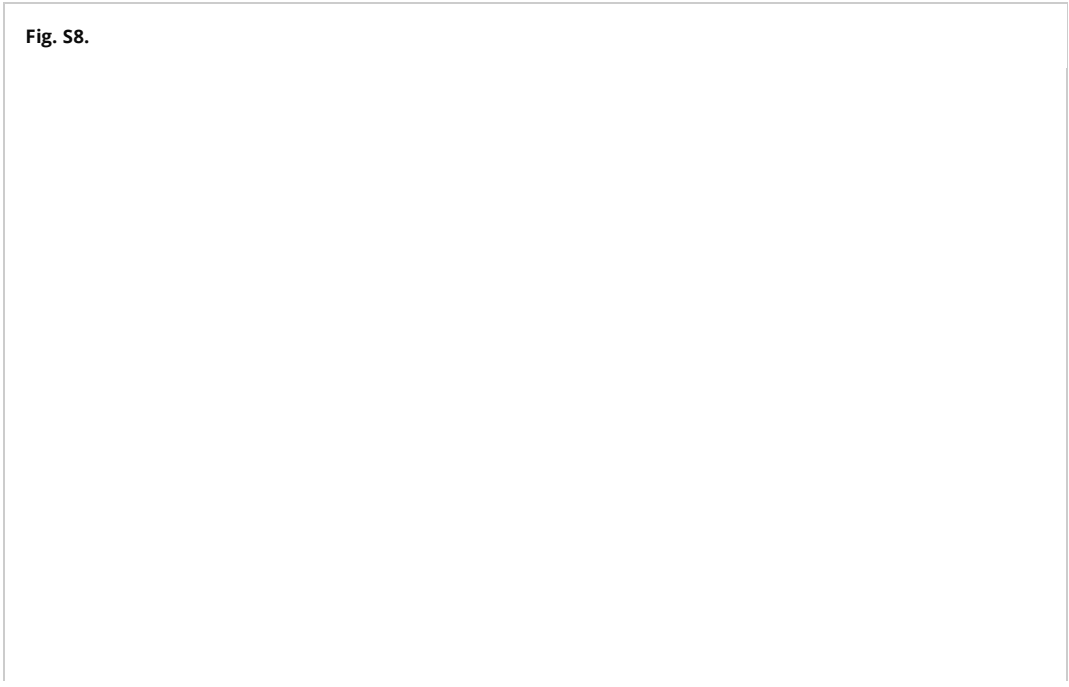

Average tetrahedrality $\langle q \rangle$ of the bilayers B1 through B5 as a function of system temperature. (Inset) A sectional view of the ice slab.

Conclusion

Both in SFG experiments and in MD simulations, a stepwise apparent blueshift in the spectra of the ice−air interface around 257 K has been observed. This feature that indicates weakening of the hydrogen bonds marks the transition to a state in which the surface layers entail a more liquid character. The relatively small temperature variation of the dangling OH in the temperature range from 235 K to 273 K suggests that the outermost layer is not changing its nature over this temperature range. Therefore, we conclude that, already at 235 K, a QLL is present on ice. This quasi-liquid water layer suddenly increases its thickness around 257 K in a discrete bilayer-by-bilayer manner. A comparison of the SFG response of ice at 270 K with that of supercooled water at the same temperature indicates that the QLL is more similar to ice than to supercooled liquid water: The QLL seems to have stronger hydrogen bonds than liquid water. This information is crucial for understanding both the surface chemistry on ice under near-freezing conditions (42–44) and the melting mechanism of the ice surface, which has important geophysical implications on the macroscopic scale of our planet, such as for glacier sliding (45).

Materials and Methods

Sample Preparation.

As described in more detail in *Supporting Information*, single crystalline ice Ih was grown by seed extraction from a melt (29). A single crystalline seed is used as the starting point. The crystallinity of the

basal or secondary prism) was cut with a band saw. The orientation of the sample was confirmed using Formvar etching (47) (2% m/v) and X-ray diffraction. Before SFG measurements, oriented samples were mounted in a homemade stainless steel sample holder and flattened with a modified microtome (using disposable diamond-coated blades; C.L Sturkey, Inc.) and a clean oxidized silicon wafer. Finally, the ice sample was annealed for at least 24 h in the closed sample holder at 253 K. All of the components that were in contact with ice (i.e., band saw blade and sample cell) were cleaned with acetone and ethanol and rinsed with deionized water. In addition, silicon wafers were heated at 500 °C.

The secondary prism ice samples were oriented with the *c* axis perpendicular to the plane formed by the incident laser light and the surface normal.

SFG Setup.

A Ti:sapphire regenerative amplifier (Spitfire Ace; Spectra-Physics) generates laser pulses (5 mJ at 1 kHz) centered at 800 nm with a pulse duration of 40 fs; 1 mJ of the laser output is used to pump a commercial optical parametric amplifier (TOPAS-C; Spectra-Physics). The signal and idler output were difference-frequency mixed in a silver gallium disulfide ($AgGaS_2$) crystal to generate IR pulses around 3,000 cm^{-1} and 3,600 cm^{-1} (FMWH ~250 cm^{-1}) with pulse energies at the sample of 3 μJ and 1.5 μJ, respectively. The visible probe pulse (20 μJ, FWHM 20 cm^{-1}) was obtained by frequency narrowing 1 mJ of the laser output in an etalon (SLS Optics Ltd.). The incident angles of the IR and visible beams were 40° and 51°, respectively, with respect to the surface normal.

The ice spectra were collected under *ssp* polarization and normalized to a nonresonant signal from a gold-coated (~100 nm) silicon wafer. The 380-μm-thick gold-coated silicon wafer (0.25 cm^2) was placed on top of the ice surface outside the ice area probed with SFG. In the SFG experiments, the infrared laser pulse is resonant with the molecular vibration. To avoid surface melting during experiments in the hydrogen-bonded region, the repetition rate of the infrared was reduced to 250 Hz and the sample was moved with a pivot crank mechanism at a speed of 2.8 cm/s. In this way, every laser shot was at a new position; after ~3 s, the laser returned back to the same position. Typical acquisition times are around 10 min. The supercooled water and ice spectra at 269 K in Fig. 7 are acquired for 60 min and 140 min, respectively.

As the cleanliness of the ice alters the premelting QLL thickness (48), we carefully checked that the ice surface is free from organic impurities by measuring the CH stretch SFG signal. No detectable C–H contamination was present, as shown in Fig. S4. The reproducibility of the spectra between different samples manifests that the surface was also free from nonorganic contaminants.

MD Simulations.

MD simulations were performed to compute the density profiles, RDFs, and tetrahedral order parameter of ice surfaces. To examine whether different MD setups affect the density profiles of ice, we performed two MD simulations with different cell size and different number of water molecules. The TIP4P/Ice model (36) was used for water molecules. The details of the MD simulations are given in *Supporting Information*. The obtained 40-ns MD trajectories were used to compute density profiles, radial distributions function, and tetrahedral order parameter.

Subsequently, we computed SFG spectra of ice. Because the OH stretch vibrational mode cannot be described by the fixed-body water model and the dipole moment of water cannot be described accurately with a nonpolarizable model, the fixed-body and nonpolarizable TIP4P/Ice water model is not applicable to the SFG spectra calculation. Instead, we used the polarizable and flexible-body charge response kernel (CRK) water model (49). The simulation details can be found in *Supporting Information*. The obtained total

Calculation of SFG Spectra.

The *ssp* polarized SFG intensity, $I_{SFG}(\omega)$, is given by the square of the *xxz* component of the second-order nonlinear susceptibility $\chi_{xxz}^{(2)}(\omega)$, where the *xy* plane is parallel to the surface and the *z* axis forms the normal to the surface. The $\chi^{(2)}(\omega)$ is composed of a vibrationally resonant part $\chi^{(2),R}(\omega)$ and a nonresonant part $\chi^{(2),NR}$

$$\chi^{(2)}(\omega) = \chi^{(2),R}(\omega) + \chi^{(2),NR}. \quad [1]$$

The $\chi_{xxz}^{(2),R}(\omega)$ can be accessed by calculating the time correlation function of the *z* component of the dipole moment (M_z) and the *xx* component of the polarizability (A_{xx}) as (50)

$$\chi_{xxz}^{R}(\omega_{IR}) = \frac{i\omega_{IR}}{k_B T}\int_0^{\tau_c} dt \exp(i\omega_{IR} t)\langle A_{xx}(t) M_z(0)\rangle, \quad [2]$$

where ω_{IR} is the IR frequency, k_B is the Boltzmann constant, and T is the temperature; τ_c was set to 1.2 ps. The polarizability and dipole moment were calculated with the local field correction using the CRK model (49). To suppress the noise of the time correlation function, Eq. **2**, due to the limited length of the MD trajectories, we used the damping treatment on the distant intermolecular correlation (51), with a cutoff distance of 5.6 Å O−O distance. To be consistent with experimental data, $\chi^{(2),NR} = -0.15$ was used for constructing the $I_{SFG}(\omega)$ spectra in Fig. 5.

SI Materials and Methods

Growth of Single Crystalline Ice.

The single crystal ice boule growth method is based on withdrawing a single crystalline seed from a liquid water melt (29). A single crystal seed is frozen onto a copper pin, kept at 248 K, which is attached to a Peltier element with liquid back-cooling. As soon as the seed and the copper pin are well connected, the surface of the seed is melted with a heat gun, and formed water drops are blown away with N_2. With the surface of the seed still being liquid, the copper pin with the seed is quickly lowered to make contact between the seed and a constantly stirred melt, kept at 272.85 K, and allowed to grow in the melt for half an hour. After confirming that the seed is growing in the melt, the seed is slowly raised at 5 mm/h to allow the boule to grow in diameter and in length. This produces a 30-mm-long cylindrical single crystalline boule with 60- to 90-mm diameter in 6 h to 7 h (Fig. S1*A*). The initial seed was obtained from a modified Bridgman method (23). Alternatively, it could, for example, be obtained from a free-growing ice dendrite (29).

Single crystallinity of the boule was confirmed on a Rigsby stage between two crossed polarizers (46) (Fig. S1*B*). Slices of these single crystalline boules were used as seeds for the subsequent production of single crystalline ice boules, or as samples. Those slices were cut from the boule with a band saw, at specific roll and azimuth angles, to orient the *c*-axis perpendicular to the cross-section of the slice. The cutting angles were obtained from the geometrical analysis of the pits generated from Formvar etching, where the shape of the etch pit represents the orientation of the *c* axis in the slide (47, 52, 53). Fig. S2 shows images after formvar etching of the basal, primary, and secondary prism plane, which has been confirmed with X-ray diffraction (see *X-Ray Characterization*).

Ice Sample Cell.

For the SFG measurements, a copper plate was cooled down to 223 K with a Peltier element. The heat generated by the Peltier was transferred into a water/polyglycol mixture cycling through an open bath chiller set at 255 K. After reaching the desired temperature, the sample was kept for at least 30 min before

then the samples were further flattened with a silicon wafer; thirdly, the gold reference was placed on top of the ice; and, finally, the cell was closed with a CaF_2 window and annealed for one night. The small piece (~0.5 cm × 0.5 cm × 0.03 cm) of gold-coated silicon wafer was used as reference in the SFG experiments to determine the frequency dependence of the IR. The cell was constantly moved in a circular motion on the copper plate by a motorized pivot crank mechanism at a speed of ~30 mm s^{-1}.

X-Ray Characterization.

The structure and orientation of single crystal ice samples were studied by X-ray diffraction. X-rays from a Cu Kα (wavelength 1.54 Å) rotating anode source (Rigaku MicroMax 007 X-ray generator) with curved multilayer optics (Osmic Confocal Max-Flux) are collimated by a set of two four-jaw apertures. Measurements were conducted on a self-constructed six-circle diffractometer using the standard angle convention (54). Ice crystals were mounted inside a sealed sample cell on a copper disk, cooled to ~253 K. Full access to the sample surface by the incident and scattered X-ray beam is provided by a transparent Kapton dome (foil thickness 25 μm). X-rays are detected at a sample-detector distance of 57 cm by a microstrip solid-state detector (Dectris Mythen).

To determine the surface orientation of ice samples, previously oriented by the Formvar etch technique (Fig. S2), the positions of multiple Bragg reflections were recorded (Table S1). The widths of the measured rocking curves are limited by the instrumental resolution (Fig. S3). Miscuts and crystal orientations determined by X-ray diffraction with respect to the alignment using the Formvar etch technique are summarized in Table S2.

SI Additional SFG Results

Ice melts due to the absorption of the infrared probe light when probed in the hydrogen-bonded region. A dramatic decrease of the signal intensity is observed when the sample is not moving. To avoid melting, the sample was moved and, for the bonded OH region, the repetition rate of the infrared pulse was reduced to 250 Hz so that every laser shot appears on a fresh spot. As the absorption is less at higher frequency, a repetition rate of 1 kHz could be used for the SFG measurement in the free OH stretch frequency range (~3,700 cm^{-1}).

Fig. S4 shows that, following this procedure, the SFG spectrum at 235 K in the hydrogen-bonded range is stable over at least 6 h: The spectrum after 6 h of continuous irradiation is identical to the initial spectrum. Moreover, a repetition rate of 250 Hz and 164 Hz gave identical results. The stability of the signal shown in Fig. S4 proves that the sample is not damaged by the laser. Moreover, the spectra in Fig. S4 show no CH stretch vibration; the CH stretch modes of hydrocarbon contamination are normally observed in the frequency range of 2,800 $cm^{-1} < \omega <$ 3,000 cm^{-1}. The absence of a signal in this frequency range indicates that the sample has no contamination or contamination that is less than the detection limit.

Fig. S5*A* depicts SFG spectra of the secondary prism face as a function of temperature. The intensity decreases as the temperature increases, as was observed for the basal plane. The spectral first moment presents a more gradual shift to higher frequencies at 257 K in comparison with the basal plane (Fig. 2*B*). Moreover, after fitting the data with a linear combination of the spectrum at 235 K and the one at 269 K, the contribution of the 235 K spectrum linearly decreases by increasing temperature, whereas the contribution from the 269 K spectrum may increase around 257 K (Fig. S5*B*).

SI MD Simulation for Computing Density Profile, Radial Distribution

Functions, Tetrahedrality Parameter, and SFG Spectra of Ice

MD Simulation 1.

To examine the effects of the different MD approaches on the ice density profile, we performed two independent MD simulations. The methodology of the MD simulation for the ice surface was essentially the same as in ref. 35. For MD simulation 1, a slab of proton-disordered ice Ih consisting of 1,120 H_2O molecules was prepared with the Monte Carlo method (55) in a rectangular simulation box of 31.44 Å × 31.11 Å × 40 Å. The ice forms a slab of ∼34 Å thickness, with two basal face surfaces normal to the *z* axis.

For equilibrating the systems generated by the Monte Carlo simulation, first simulations in the isothermal-isobaric ensemble (NPT) were carried out using the TIP4P/Ice model (36). The periodic boundary condition was used for the *x*, *y*, and *z* directions. The electrostatic interactions were calculated with the Ewald summation method. In the NPT equilibration process, semiisotropic pressure coupling to control the pressure in the *xy* and *z* directions separately at $P = 1$ atm was employed using the Parrinello−Rahman barostat (56), and the temperature was controlled with the Nosè−Hoover thermostat (57, 58). The target temperatures were set to 230, 240, 250, 260, 270, and 280 K. After the NPT equilibration for 1 ns, we elongated the *z* length of the cell to 150 Å and carried out further equilibration in the canonical ensemble (NVT) for 10 ns. These equilibrations were conducted with GROMACS package (version 4.6.1) (59). For all of simulation 1, the equation of motion has been integrated with a time step of $\Delta t = 2$ fs.

MD Simulation 2.

In the second set of MD simulations, a slab of proton-disordered ice Ih consisting of 1,536 TIP4P/Ice H_2O molecules was prepared following the same procedure outlined in *MD Simulation 1*. The initial sizes of the periodic simulation box were 36 Å × 23.38 Å × 58.56 Å for the basal plane and 54 Å × 31.1769 Å × 29.28 Å for the secondary prism plane. To take into account thermal expansion, we performed simulations of bulk ice in the NPT ensemble at each target temperature, 230, 240, 250, 260, 270, and 272 K, at a pressure of 1 bar. We then generated a slab for each sample equilibrated in the NPT ensemble by introducing a vacuum layer of ∼2 nm, and we ran 10-ns equilibration in the NVT ensemble, in which the temperature was controlled by stochastic velocity rescaling (60) with a coupling constant of 2 ps. Hence we performed 40-ns-long production runs, also in the NVT ensemble.

In these MD simulations, the equations of motion were integrated with a time step $\Delta t = 1$ fs. The long-range electrostatic interactions were calculated using smooth particle mesh Ewald summation. The simulation has been conducted with DL_POLY software (61). We obtained nearly identical results as for the density profiles and the tetrahedrality parameters of ice for MD simulations 1 and 2.

MD Simulation for SFG Spectra Calculation.

Sequentially, we computed the SFG spectra of ice. For computing SFG spectra we used the polarizable and flexible-body CRK water model (49) instead of the TIP4P/ice model. The latter is a fixed-body and nonpolarizable water model, and not suitable for the SFG calculation. The CRK model has been frequently used for computing the OH stretch SFG spectra, which show good agreement with the experimental data. Starting from 16 different molecular configurations of ice generated with the TIP4P/Ice model (MD simulation 1), we ran 1-ps NVT MD simulation with the CRK water model for each configuration. The equation of motion was integrated with a time step of $\Delta t = 0.61$ fs. To control the system temperature, we used the Berendsen thermostat (62) with coupling constant of 0.4 ps. Sequentially, 60 ps NVE runs were performed for each of the 16 configurations. This procedure generated a total 960 ps MD trajectory. The average temperatures over the total 960 ps NVE MD trajectory were 230.25, 240.17, 250.19, 260.61, and

270.49 K. This 960 ps MD trajectory was used for computing the time correlation functions of the dipole moment and polarizability.

CRK vs. Quantum Mechanics/Molecular Mechanics Approach for Computing SFG Spectra.

The present simulation of SFG spectra was carried out with the classical CRK model of water, whereas our previous work on ice surface used quantum mechanics/molecular mechanics (QM/MM) calculation of dipole and polarizability (34, 35). Therefore, we discuss here the differences between the calculation methods and the performance. The classical model was used to lower the computational cost, but, arguably, the present simulation is adequate enough to prove the relation between the surface premelting and the peak shift of the SFG signal.

The principal advantage of using the QM/MM calculation is to reproduce the remarkably strong SFG signal of ice surface in the hydrogen-bonding region (~3,200 cm^{-1}) in comparison with the dangling OH (~3,700 cm^{-1}); this is because the hydrogen-bonded OH vibrations are strongly influenced by the charge transfer, which is not fully described by the classical model. We note that the previous works with the QM/MM calculation also used classical polarizable simulation to generate MD trajectories, and thus the structure of the ice surface was essentially equivalent. The difference only lies in the evaluation method of dipole and polarizability in the nonlinear susceptibility. The surface premelting of ice is captured by the present simulation as well, as discussed in *Tetrahedrality Parameter* $\langle q \rangle$. Such apparent structural change is reflected in the calculated SFG spectra.

Tetrahedrality Parameter $\langle q \rangle$.

The surface premelting is further demonstrated by introducing the average tetrahedrality $\langle q \rangle$, an index of lattice disorder, where $\langle q \rangle = 1$ stands for complete tetrahedral order, and $\langle q \rangle = 0$ indicates a random structure (35). Fig. S8 shows the order parameter $\langle q \rangle$ calculated with the CRK model with varying depth (bilayer number) and temperature. This figure shows that the interior of ice (e.g., B5 layer) at 230 K has an ordered structure with $\langle q \rangle \approx 0.96$, whereas the $\langle q \rangle$ value decreases near the surface, indicating the surface disorder of ice. With increasing temperature, the $\langle q \rangle$ value quickly decreases at about 270 K to ~280 K, implying the surface melting of ice. The structural transition is signified in the peak shift of the calculated SFG spectra in Fig. 5*B*, as the SFG is sensitive to a few bilayers of ice.

Finally we would like to note that these data were generated based on the layer-by-layer definition. These can be also plotted based on the recently proposed coarse-graining instantaneous liquid interface.

Density Profiles.

Density profiles (Fig. S6) were computed by averaging over a 40 ns trajectory of systems containing 1,536 molecules (*MD Simulation 2*). Profiles are taken by moving perpendicularly to the slab surfaces, namely along the [0001] direction for the basal plane and the [$\bar{1}2\bar{1}0$] direction for the secondary prism plane. Each point of the profile is obtained by convoluting the instantaneous atomic positions with a normalized triangular weighting function with width 0.105 nm, for snapshots taken every 10 ps from the trajectory. The error bars represent the SD.

The double peak in the density profiles of the basal plane slab (Fig. S6*A*) is a fingerprint of crystalline ice bilayers: Disappearance of the double peak indicates that a bilayer is disordered and possibly molten. We observe that, in the simulations below 270 K, the outermost bilayers do not exhibit the double peak, whereas, at 270 K and above, the first and the second outermost bilayers lose this feature. At the same time, the minimum separating the first and second bilayer rises, indicating an increased exchange of molecules. This transition occurs sharply between 260 K and 270 K.

The second prism slab is made of equidistant single layers (Fig. 1). The monolayer structure is also visible in the density profiles in Fig. S6*B*. The ice melting transition is less sharp. The envelope of the density profiles evolves smoothly from a rectangular shape to an ellipsoidal one, with a gradual decrease of the distance between peaks and valleys from the outer layers inward.

RDFs.

Comparison of the RDF of each bilayer slab to those of the reference systems' bulk ice and bulk water provides compelling evidence of the sharp melting transition occurring between 260 K and 270 K in the MD simulations. To compute the RDF of the reference systems, we performed MD simulations in the NPT ensemble at the target temperatures of 230 K to 272 K for a liquid water model consisting of 480 molecules and an ice Ih model consisting of 1,536 molecules. In these simulations, we follow the same protocol described in *MD Simulation 2*.

Fig. S7 shows three RDFs. In Fig. S7*A*, the temperature dependence of the RDFs for the reference systems is shown. Also, the characteristic differences between the RDFs for the ice Ih and for the liquid are shown, to be compared with the RDFs shown in Fig. S7 *B* and *C*. The RDFs are shown resolved by bilayers. Therefore, the RDFs are obtained in three steps. In a first step based on the density profiles in Fig. S6*A*, parameters for distinguishing the first and the second bilayers are obtained. They are then used to create different RDFs resolved in bilayers. In a last step, the RDFs for the bilayers slices are scaled to the bulk according to

$$\kappa(r) = \frac{l_s}{\Delta z} \cdot \begin{cases} 1 - \frac{1}{2}\frac{r}{\Delta z}, & r \le \Delta z \\ \frac{1}{2}\frac{r}{\Delta z}, & r > \Delta z \end{cases},$$

where Δz is the width of the bilayer slice, l_s is the full length of the simulation box in the [0001] direction, and the RDFs are scaled by division through $\kappa(r)$ (63).

The RDFs of the first bilayer (Fig. S7*B*) of the basal plane show liquid-like behavior (Fig. S7*A*). Notwithstanding, the RDFs of the second bilayer exhibit a rather sharp transition between 260 K and 270 K from an ice-like to a liquid-like RDF.

Acknowledgments

We thank Joan Fitzpatrick, Frederik Fleißner, Rémi Khatib, Hailong Li, Xiao Ling, Sapun Parekh, and Marialore Sulpizi for discussions and Florian Gericke for excellent technical support. The Max Planck Graduate Center is acknowledged for funding.

Supporting Information

Supporting Information (PDF)
Supporting Information

DOWNLOAD | 821.40 KB

References

1 M Faraday, On regelation, and on the conservation of force. *Philos Mag* **17**, 162–169 (1859).
Crossref | Google Scholar

2 R Rosenberg, Why is ice slippery? *Phys Today* **58**, 50–55 (2005).

3 JG Dash, AW Rempel, J Wettlaufer, The physics of premelted ice and its geophysical consequences. *Rev Mod Phys* **78**, 695–741 (2006).

Crossref | Google Scholar

4 R Lipowsky, Critical surface phenomena at first-order bulk transitions. *Phys Rev Lett* **49**, 1575–1578 (1982).

Crossref | Google Scholar

5 BF Henson, LF Voss, KR Wilson, JM Robinson, Thermodynamic model of quasiliquid formation on H_2O ice: Comparison with experiment. *J Chem Phys* **123**, 144707 (2005).

Crossref | PubMed | Google Scholar

6 CL Bishop, et al., On thin ice: Surface order and disorder during pre-melting. *Faraday Discuss* **141**, 277–292, and discussion (2009) 141:309–346 (2009).

Crossref | PubMed | Google Scholar

7 MM Conde, C Vega, A Patrykiejew, The thickness of a liquid layer on the free surface of ice as obtained from computer simulation. *J Chem Phys* **129**, 014702 (2008).

Crossref | PubMed | Google Scholar

8 G-J Kroes, Surface melting of the (0001) face of TIP4P ice. *Surf Sci* **275**, 365–382 (1992).

Crossref | Google Scholar

9 H Asakawa, G Sazaki, K Nagashima, S Nakatsubo, Y Furukawa, Prism and other high-index faces of ice crystals exhibit two types of quasi-liquid layers. *Cryst Growth Des* **15**, 3339–3344 (2015).

Crossref | Google Scholar

10 H Bluhm, DF Ogletree, CS Fadley, Z Hussain, M Salmeron, The premelting of ice studied with photoelectron spectroscopy. *J Phys Condens Matter* **14**, L227–L233 (2002).

Crossref | Google Scholar

11 H-J Butt, A Döppenschmidt, G Hüttl, E Müller, OI Vinogradova, Analysis of plastic deformation in atomic force microscopy: Application to ice. *J Chem Phys* **113**, 1194–1203 (2000).

Crossref | Google Scholar

12 A Döppenschmidt, H-J Butt, Measuring the thickness of the liquid-like layer on ice surfaces with atomic force microscopy. *Langmuir* **16**, 6709–6714 (2000).

Crossref | Google Scholar

13 H Dosch, A Lied, J Bilgram, Glancing-angle X-ray scattering studies of the premelting of ice surfaces. *Surf Sci* **327**, 145–164 (1995).

Crossref | Google Scholar

14 Y Furukawa, M Yamamoto, T Kuroda, Ellipsometric study of the transition layer on the surface of an ice crystal. *J Cryst Growth* **82**, 665–677 (1987).

Crossref | Google Scholar

15 MP Goertz, X Y Zhu, JE Houston, Exploring the liquid-like layer on the ice surface. *Langmuir* **25**, 6905

Crossref | PubMed | Google Scholar

16 A Lied, H Dosch, JH Bilgram, Surface melting of ice Ih single crystals revealed by glancing angle x-ray scattering. *Phys Rev Lett* **72**, 3554–3557 (1994).

Crossref | PubMed | Google Scholar

17 G Sazaki, S Zepeda, S Nakatsubo, M Yokomine, Y Furukawa, Quasi-liquid layers on ice crystal surfaces are made up of two different phases. *Proc Natl Acad Sci USA* **109**, 1052–1055 (2012).

Crossref | PubMed | Google Scholar

18 Y Li, GA Somorjai, Surface premelting of ice. *J Phys Chem C* **111**, 9631–9637 (2007).

Crossref | Google Scholar

19 YR Shen, Surface properties probed by second-harmonic and sum-frequency generation. *Nature* **337**, 519–525 (1989).

Crossref | Google Scholar

20 X Wei, PB Miranda, YR Shen, Surface vibrational spectroscopic study of surface melting of ice. *Phys Rev Lett* **86**, 1554–1557 (2001).

Crossref | PubMed | Google Scholar

21 X Wei, PB Miranda, C Zhang, YR Shen, Sum-frequency spectroscopic studies of ice interfaces. *Phys Rev B* **66**, 085401 (2002).

Crossref | Google Scholar

22 IL Barnett, H Groenzin, MJ Shultz, Hydrogen bonding in the hexagonal ice surface. *J Phys Chem A* **115**, 6039–6045 (2011).

Crossref | PubMed | Google Scholar

23 PJ Bisson, MJ Shultz, Hydrogen bonding in the prism face of ice I(h) via sum frequency vibrational spectroscopy. *J Phys Chem A* **117**, 6116–6125 (2013).

Crossref | PubMed | Google Scholar

24 H Groenzin, I Li, V Buch, MJ Shultz, The single-crystal, basal face of ice I(h) investigated with sum frequency generation. *J Chem Phys* **127**, 214502 (2007).

Crossref | PubMed | Google Scholar

25 H Groenzin, I Li, MJ Shultz, M Jane, Sum-frequency generation: Polarization surface spectroscopy analysis of the vibrational surface modes on the basal face of ice I(h). *J Chem Phys* **128**, 214510 (2008).

Crossref | PubMed | Google Scholar

26 R Rossend, KB Møller, JT Hynes, Hydrogen bond dynamics in water and ultrafast infrared spectroscopy. *J Phys Chem A* **106**, 11993–11996 (2002).

Crossref | Google Scholar

27 CP Lawrence, JL Skinner, Vibrational spectroscopy of HOD in liquid D_2O. III. Spectral diffusion, and hydrogen-bonding and rotational dynamics. *J Chem Phys* **118**, 264–272 (2003).

Crossref | Google Scholar

28 JD Bernal, RH Fowler, A theory of water and ionic solution, with particular reference to hydrogen and hydroxyl ions. *J Chem Phys* **1**, 515–548 (1933).

Crossref | Google Scholar

29 DVDS Roos, Rapid production of single crystals of ice. *J Glaciol* **14**, 325–328 (1975).

Crossref | Google Scholar

30 A Higashi, M Oguro, A Fukuda, Growth of ice single crystals from the melt, with special reference to dislocation structure. *J Cryst Growth* **3**, 728–732 (1968).

Crossref | Google Scholar

31 J Czochralski, A new method for the measurement of the crystallization rate of metals. *Z Phys Chem* **92**, 219–221 (1918).

Crossref | Google Scholar

32 GP Rigsby, Crystal fabric studies on Emmons Glacier Mount Rainier, Washington. *J Geol* **59**, 590–598 (1951).

Crossref | Google Scholar

33 MJ Shultz, P Bisson, H Groenzin, I Li, Multiplexed polarization spectroscopy: Measuring surface hyperpolarizability orientation. *J Chem Phys* **133**, 054702 (2010).

Crossref | PubMed | Google Scholar

34 T Ishiyama, A Morita, A direct evidence of vibrationally delocalized response at ice surface. *J Chem Phys* **141**, 18C503 (2014).

Crossref | PubMed | Google Scholar

35 T Ishiyama, H Takahashi, A Morita, Origin of vibrational spectroscopic response at ice surface. *J Phys Chem Lett* **3**, 3001–3006 (2012).

Crossref | PubMed | Google Scholar

36 JLF Abascal, E Sanz, R García Fernández, C Vega, A potential model for the study of ices and amorphous water: TIP4P/Ice. *J Chem Phys* **122**, 234511 (2005).

Crossref | PubMed | Google Scholar

37 JF van der Veen, Melting and freezing at surfaces. *Surf Sci* **433-435**, 1–11 (1999).

Crossref | Google Scholar

38 QS Mei, K Lu, Melting and superheating of crystalline solids: From bulk to nanocrystals. *Prog Mater Sci* **52**, 1175–1262 (2007).

Crossref | Google Scholar

39 AWD van der Gon, JM Gay, JWM Frenken, JF van der Veen, Order-disorder transitions at the Ge (111) surface. *Surf Sci* **241**, 335–345 (1991).

Crossref | Google Scholar

40 X Wei, YR Shen, Motional effect in surface sum-frequency vibrational spectroscopy. *Phys Rev Lett* **86**, 4799–4802 (2001).

41 A Nilsson, LGM Pettersson, The structural origin of anomalous properties of liquid water. *Nat Commun* **6**, 8998 (2015).

Crossref | PubMed | Google Scholar

42 JPD Abbatt, Interactions of atmospheric trace gases with ice surfaces: Adsorption and reaction. *Chem Rev* **103**, 4783–4800 (2003).

Crossref | PubMed | Google Scholar

43 T Bartels-Rausch, et al., A review of air–ice chemical and physical interactions (AICI): Liquids, quasi-liquids, and solids in snow. *Atmos Chem Phys* **14**, 1587–1633 (2014).

Crossref | Google Scholar

44 TD Shepherd, MA Koc, V Molinero, The Quasi-liquid layer of ice under conditions of methane clathrate formation. *J Phys Chem C* **116**, 12172–12180 (2012).

Crossref | Google Scholar

45 KM Cuffey, H Conway, B Hallet, AM Gades, CF Raymond, Interfacial water in polar glaciers and glacier sliding at −17°C. *Geophys Res Lett* **26**, 751–754 (1999).

Crossref | Google Scholar

46 CCJ Langway, *Ice Fabrics and the Universal Stage* (US Army Snow Ice Permafrost Res Establ, Wilmette, IL), Tech Rep 62. (1958).

Google Scholar

47 DVDS Roos, Two-dimensional grain growth in ice. *J Glaciol* **6**, 411–420 (1966).

Crossref | Google Scholar

48 JS Wettlaufer, Impurity effects in the premelting of ice. *Phys Rev Lett* **82**, 2516–2519 (1999).

Crossref | Google Scholar

49 T Ishiyama, A Morita, Analysis of anisotropic local field in sum frequency generation spectroscopy with the charge response kernel water model. *J Chem Phys* **131**, 244714 (2009).

Crossref | PubMed | Google Scholar

50 A Morita, JT Hynes, A theoretical analysis of the sum frequency generation spectrum of the water surface. II. Time-dependent approach. *J Phys Chem B* **106**, 673–685 (2002).

Crossref | Google Scholar

51 Y Nagata, S Mukamel, Vibrational sum-frequency generation spectroscopy at the water/lipid interface: Molecular dynamics simulation study. *J Am Chem Soc* **132**, 6434–6442 (2010).

Crossref | PubMed | Google Scholar

52 MJ Shultz, A Brumberg, PJ Bisson, R Shultz, Producing desired ice faces. *Proc Natl Acad Sci USA* **112**, E6096–E6100 (2015).

Crossref | PubMed | Google Scholar

53 K Higuchi, The erching of ice crystals. *Acta Metall* **6**, 636–642 (1958).

54 M Lohmeier, E Vlieg, Angle calculations for a six-circle surface X-ray diffractometer. *J Appl Cryst* **26**, 706–716 (1993).

Crossref | Google Scholar

55 V Buch, P Sandler, J Sadlej, Simulations of H_2O solid, liquid, and clusters, with an emphasis on ferroelectric ordering transition in hexagonal ice. *J Phys Chem B* **102**, 8641–8653 (1998).

Crossref | Google Scholar

56 M Parrinello, A Rahman, Polymorphic transitions in single crystals: A new molecular dynamics method. *J Appl Phys* **52**, 7182–7190 (1981).

Crossref | Google Scholar

57 WG Hoover, Canonical dynamics: Equilibrium phase-space distributions. *Phys Rev A Gen Phys* **31**, 1695–1697 (1985).

Crossref | PubMed | Google Scholar

58 S Nosé, A unified formulation of the constant temperature molecular dynamics methods. *J Chem Phys* **81**, 511–519 (1984).

Crossref | Google Scholar

59 B Hess, C Kutzner, D van der Spoel, E Lindahl, GROMACS 4: Algorithms for highly efficient, load-balanced, and scalable molecular simulation. *J Chem Theory Comput* **4**, 435–447 (2008).

Crossref | PubMed | Google Scholar

60 G Bussi, D Donadio, M Parrinello, Canonical sampling through velocity rescaling. *J Chem Phys* **126**, 014101 (2007).

Crossref | PubMed | Google Scholar

61 IT Todorov, W Smith, MT Dove, DL_POLY_3: New dimensions in molecular dynamics simulations via massive parallelism. *J Mater Chem* **16**, 1911–1918 (2006).

Crossref | Google Scholar

62 HJC Berendsen, JPM Postma, WF van Gunsteren, A DiNola, JR Haak, Molecular dynamics with coupling to an external bath Molecular dynamics with coupling to an external bath. *J Chem Phys* **81**, 3684–3690 (1984).

Crossref | Google Scholar

63 M Jochum, D Andrienko, K Kremer, C Peter, Structure-based coarse-graining in liquid slabs. *J Chem Phys* **137**, 064102 (2012).

Crossref | PubMed | Google Scholar

64 AD Fortes, et al., No evidence for large-scale proton ordering in Antarctic ice from powder neutron diffraction. *J Chem Phys* **120**, 11376–11379 (2004).

Crossref | PubMed | Google Scholar

Further reading in this issue

RESEARCH ARTICLE | DECEMBER 22, 2016 |

Microbial competition in porous environments can select against rapid biofilm growth

Katharine Z. Coyte, Hervé Tabuteau, [...] William M. Durham

RESEARCH ARTICLE | DECEMBER 27, 2016 |

Achromatopsia mutations target sequential steps of ATF6 activation

Wei-Chieh Chiang, Priscilla Chan, [...] Jonathan H. Lin

RESEARCH ARTICLE | JANUARY 9, 2017 |

Climatic regulation of the neurotoxin domoic acid

S. Morgaine McKibben, William Peterson, [...] Angelicque E. White

Trending

RESEARCH ARTICLE | JUNE 25, 2025 |

Generative AI without guardrails can harm learning: Evidence from high school mathematics

While generative AI has been shown to enhance productivity, its influence on learning new skills remains unclear. Our...

Hamsa Bastani, Osbert Bastani, [...] Rei Mariman

RESEARCH ARTICLE | MAY 19, 2026 |

Large language models pass a standard three-party Turing test

The Turing test asks whether a machine can imitate human behavior so well that another human cannot reliably tell the...

Cameron R. Jones and Benjamin K. Bergen

RESEARCH ARTICLE | MAY 21, 2026 |

Cultural evolution of beauty standards

Who gets to be beautiful, and who decides? The media and fashion industry set aspirational body standards with...

Louis Boucherie, Sagar Kumar, [...] Karolina Śliwa